Gong, Y., Zhang, B., Mukhopadhyay, S., & Hallett, S. R. (2018). Experimental study on delamination migration in multidirectional laminates under mode II static and fatigue loading, with comparison to mode I. *Composite Structures*, *201*, 683-698. https://doi.org/10.1016/j.compstruct.2018.06.081

Experimental study on delamination migration in multidirectional laminates under mode II static and fatigue loading, with comparison to mode I

Yu Gong[a,b,*], Bing Zhang[b], Supratik Mukhopadhyay[b], Stephen R. Hallett[b]

[a] College of Aerospace Engineering, Chongqing University, Chongqing 400044, China

[b] Bristol Composites Institute (ACCIS), University of Bristol, Queen's Building, University Walk, Bristol BS8 1TR, UK

Abstract:

This paper presents an experimental investigation to better understand the mechanisms of delamination migration in multidirectional End Loaded Split (ELS) specimens. A stacking sequence susceptible to delamination migration was selected for this study and subjected to pure mode II static and fatigue loading. The static and fatigue results gave comparable migration mechanisms, however, differences were noted regarding the damage sequence, the fracture surface, the migration angle and the horizontal distances of migrated location to the front of pre-crack. Scanning Electron Microscopy (SEM) results indicated that fibre imprints and cusps were two dominant micro-features on the fracture surfaces for all specimens. Interactions between delamination and ply splits were observed and confirmed by X-ray CT scanning. Furthermore, comparison was made to understand the effects of loading modes (mode I and II) on delamination migration.

***Keywords*:** Carbon fibre; Delamination; Transverse cracking; Mechanical testing

1 Introduction

Delamination is a major weakness of high performance composite laminates or adhesively bonded structures [1-3]. It poses a great threat to the integrity of laminated structures as it normally develops in the interior of laminates at relatively lower stress levels in comparison to fibre failure. Multidirectional laminates are more widely used in industrial composite structures than unidirectional ones [4-6], to achieve comparable mechanical properties along all the in-plane directions. However, in multidirectional laminates, delamination in the initial fracture plane is prone

* Corresponding author.
E-mail address: gongyu@cqu.edu.cn (Y. Gong).

to drifting in to adjacent interlaminar interfaces via transverse matrix cracks (ply splits), known as migration [7]. The migration phenomenon makes it difficult to characterise interlaminar fracture toughness using conventional standards, which have been well established for single delamination tests. Furthermore, delamination migration is not only difficult to avert, but it may also be seen to take place in various load scenarios [7-9], e.g. low-velocity impact [9], debonding between the flange and skin of an integrally stiffened panel [8], delamination growth emanating from embedded defects and notches [10-12] and shear loading on non-unidirectional laminates [13-17]. In regard to numerical simulation, numerous studies have focused on the modelling of delamination by using the virtual crack closure technique [18-20] and cohesive zone models [21, 22]. In order to predict delamination migration, advanced numerical techniques, such as the extended [23-25] and augmented [26] finite element methods (FEMs) and Floating Node Method (FNM) [27], have been proposed. However, there is still a lack of in-depth knowledge on the fundamental driving mechanisms for delamination migration.

There only exists a limited number of studies on delamination migration in the open literature. A special experimental set-up was developed by Ratcliffe et al. [28] to isolate a single complete migration event after the onset of delamination growth. A cross-ply specimen was also employed to allow the delamination growth and migration to occur uniformly across the specimen width, creating a benchmark case for advanced modelling techniques developed in Refs. [29-31]. To avoid the unstable migration, modifications to the stacking sequence and polytetrafluoroethylene (PTFE) insert location were subsequently employed to promote stable delamination-growth onset and migration [32]. Instead of a symmetric or antisymmetric stacking sequence, Pernice et al. [33] investigated delamination migration via asymmetric 0°/60° and 0°/75° interfaces; shear stress sign at the delamination front was obtained via a simple FE model in order to qualitatively interpret experimental results. Canturri et al. [34] reported a numerical study on the incidence of migration under mixed mode II/III loading. However, the aforementioned studies were mainly focused on

static delamination migration. Hence, Gong et al. [35] extended the study on delamination migration to fatigue loading, specifically via mode I cyclic tests on specimens with +θ/-θ interfaces; with θ equal to 60° or 70°. Mode I delamination has received most attention in the literature because mode I toughness normally features a lower value than other modes [36]. In practical application, most of composite structures are susceptible to bending, which means that if cracking occurs at interfaces between different oriented layers, it may dominantly propagate by a shearing mode, i.e. mode II. Therefore, studies on mode II delamination migration are imperative for engineers.

This study investigates delamination migration mechanisms in specimens with +75°/-75° and +60°/-60° interfaces under pure mode II loading. The organisation of the paper is as follows: Firstly, Sections 2 and 3 details the specimen configuration and experimental set-up for static and fatigue mode II tests. Section 4 then presents experimental results and compares the delamination migration mechanisms of static and fatigue mode II cases. In conjunction with the previous work on mode I case [35], this paper also gives a comparative analysis and summary of delamination migration mechanisms in multidirectional laminates under mode I and II loading.

2 Specimen configurations

The specimens used here for mode II characterisation were designed and manufactured following the same procedures as reported in Ref. [35] for mode I specimens. For completeness, the geometry and layups of the mode II specimens are briefly repeated here. The selected layup is [$+\theta_2$ $-\theta_2$ 0 $-\theta_4$ $-\alpha$ $-\theta$ $-\alpha$ 90 $-\alpha$ α 90 α θ α θ_4 0 $+\theta_2$ $-\theta_2$//$+\theta_2$ $-\theta_2$ 0 $-\theta_4$ $-\alpha$ $-\theta$ $-\alpha$ 90 $-\alpha$ α 90 α θ α θ_4 0 $+\theta_2$ $-\theta_2$], which from left to right corresponds to the lower to the upper arm of the specimen (Fig. 1a); '//' denotes the location of PTFE film insert, θ = {75°, 60°} and α = 90°-θ. This layup was selected to ensure a migration event, with reduced thermal distortions during curing and minimised un-wanted coupling effects [37]. The non-dimensional indicator D_c [38] (characterising longitudinal/transverse bending coupling) was less than 0.25 [38] for both of these two stacking sequences tested in this study. In addition, both upper and lower sub-laminates are balanced and anti-symmetric, thus it does not

exhibit bending/twisting coupling. The specimen dimensions are detailed in Fig. 1a. Hexcel HexPly® IM7/8552 carbon/epoxy prepreg with a 0.125 mm nominal ply thickness is the material system used in this study. Further details of the specimen can be found in Ref. [35].

3 Experimental method and scheme

Prior to testing, the dimensions of individual specimen were measured and recorded. The front and rear edges of each specimen were covered with a thin layer of white paint to better visualise delamination growth and migration during the tests. A calibrated scale with a 1 mm resolution was attached to each edge to aid in monitoring delamination growth and locating migration position. The ELS test set-up [40] was used here, because it introduces a relatively stable propagation for a long delamination length in comparison to the commonly used ENF (End Notched Flexture) test [41]. As shown in Fig. 1b, mechanical loading was introduced to the specimen through a loading block bonded on one side of the pre-cracked portion of the specimen with the adhesive Araldite 2011. The bonding surface of the specimen was sanded and degreased prior to bonding the block on.

All tests were carried out using a calibrated Instron 8872 servo-hydraulic testing machine equipped with a 5 kN load cell. A calibrated torque wrench was used to clamp the specimen in the fixture in a reproducible manner and a constant torque of 5 N·m was adopted in each test. Measurements of load and cross-head displacement were recorded automatically by the self-equipped sensors of the machine. Two test strategies were employed for static tests: single-step and interrupted. In the single-step tests, the specimen was loaded in displacement control at 1 mm/min until delamination has grown to the clamping region. The specimen was then unloaded at 5 mm/min. In the interrupted tests, loading of the specimens was stopped at points of interest, corresponding to load drops or delamination migration, which were chosen by referring to single-step test results.

All fatigue tests were conducted under displacement control and run at selected percentages of

the static testing displacement, corresponding to the delamination onset. The static delamination onset is identified as the point with a 5% increase in compliance from the original linear region of the static load versus displacement curve. The percentage of the static delamination onset displacement is referred to as fatigue 'severity' in this study. Interrupted fatigue tests were only conducted for specific severities and the interruption points were selected at various extents of stiffness drop, to observe the progressive damage process. Washers were inserted underneath the bolts at both sides in order to avoid the slippage of bolts during high cyclic fatigue tests. The *R* ratio, i.e. the ratio of the displacement trough to the displacement peak in a cycle is 0.1 and a frequency of 5 Hz.

After the interrupted specimens were removed from the test set-up, edge views at key stages were captured using an Olympus SZX16 microscope. The near-tip regions of selected specimens were sectioned using a water-cooled diamond-coated saw and post-mortem inspected via optical microscopy or SEM. In addition, some specimens experiencing interrupted tests were inspected using X-ray CT in order to gain an understanding of the fracture mechanisms that happened. To improve X-ray contrast, specimens were soaked in a bath of zinc iodide penetrant for 3 days. Micro X-ray CT scanning was conducted by a Nikon XTH225ST CT scanner located at the UK National Composites Centre (NCC). It has a 1 μm focal spot size and 225 kV, 225W micro-focus X-ray source. Each scanned sample was mounted on the rotation stage and positioned between the X-ray source and the 2000×2000 16 bit pixel panel detector. A voxel size of ~20μm is achieved. Post-processing on the scan results were performed using the VG studio max 2.1 and Avizo® 7 software packages.

For static tests, three specimens were tested for the single-step case and for both stacking sequences, while two and three specimens were used to perform the interrupted tests at $\theta = 75°$ and 60°, respectively. Fatigue tests were conducted at 40%, 45% and 50% severities. For the specimens with $\theta = 75°$, 40% severity was chosen for fatigue interrupted test and marked by '*' in Table 1. For

the specimens with θ = 60°, 45% severity was chosen for fatigue interrupted test and also marked by '*' in Table 1. Table 1 shows details of tested specimens.

4 Experimental results

Static and fatigue test results for these two specimen types, containing central +75°/-75° and +60°/-60° interfaces, are shown below, separately. Pictures taken from both edges and X-ray CT results are presented to provide information on the progressive damage behaviour. Further details of delamination and migration mechanisms inside the specimens are presented and discussed in what follows.

4.1 Static and fatigue tests for specimens with θ = 75°

4.1.1 Static results

Fig. 2 shows a representative load versus displacement curve recorded in single-step tests for specimens with θ = 75°. Two red circles marked in Fig. 2 indicate corresponding loads in interrupted tests. This means one interrupted-test specimen was loaded until observable initial damage, which happened before the first load drop (interrupted test 1), while the other specimen was continually loaded until the occurrence of first load drop (interrupted test 2). The load versus displacement curves of interrupted tests are shown in Fig. 3a. The front and rear views of a specimen are shown in Fig. 3b at the same scale. This applies to all the edge views presented in this paper.

Three main stages can be observed for the specimen of θ = 75° under static loading. As indicated in Fig. 2, in stage I, the load increased linearly with displacement until the initial damage. When the load reached a critical value in stage II, transverse matrix cracking developed in the adjacent lower -75° ply block due to large shear stress and weak transverse strength of the ply block. The initial delamination along the mid-plane migrated downwards through the lower -75°/+75° interface, as seen from the front side view in Fig. 3. A new delamination also occurred in the lower +75°/0° interface (see the rear side view in Fig. 3b), immediately after the initial central delamination

migrated through the matrix cracking that happened in the lower -75° and +75° ply blocks. From the front side view of interrupted test 2 in Fig. 3, it can be seen that migration developed quickly; delamination at the lower -75°/+75° interface migrated downwards and finally stayed along the lower +75°/0° interface. The significant load drop at the end of stage II also means that the failure evolution inside the specimen was unstable. With further loading in stage III, delamination remained at the lower +75°/0° interface until it propagated suddenly towards the clamping end, which caused the subsequent load drop in stage III.

Deeper understanding on damage mechanisms were obtained via X-ray CT scan results, shown in Figs. 4-5 for two static interrupted-test specimens (with $\theta = 75°$). All damage that could be observed in the CT scanned specimens is shown in these figures. All the 2D views were taken looking in the specimen thickness direction (Z-axis), as marked in Fig. 1a. A gray background is employed in some images in Figs. 4-5 to enhance contrast. Each image in the table shows damage status in a specific ply block, along with an image of the overall damage in the specimen. Damage that happened in the specimen was mostly in the form of delamination along the central +75°/-75°, adjacent lower -75°/+75° and +75°/0° interfaces, with extensive ply splits in the lower -75° ply block and lower +75° ply block spreading over the entire width of the specimen and along the length direction. After the initial damage, various damage occurred nearly simultaneously without exhibiting obvious stiffness loss. Delamination migrated through the ply splits and propagated across the width of the specimen and following the fibre direction. By comparing Fig. 4 and Fig. 5, it can be concluded that from the initial damage (the end of interrupted test 1) to the first load drop (the end of interrupted test 2), the extent of matrix cracking showed no significant increase, while apparent delamination propagation was observed at the three interfaces of interest, especially for the lower +75°/0° interfaces. The completion of whole migration event was indicated by a very significant drop in load at the end of stage II.

4.1.2 Fatigue results

For the $\theta = 75°$ case, the averaged displacement corresponding to 5% increase of compliance in the static load vs. displacement curve is 7.2 mm. Three specimens were tested at 40% severity, one tested at 45% severity and another two tested at 50% severity. Fig. 6a shows the variation of the ratio of peak load to its value for the first cycle with respect to the increasing number of cycles. For the two specimens tested at 50% severity, the peak load showed a modest decrease in the lower cycle region, while it showed a much sharper decrease after 10^4 cycles, which is caused by the delamination growth in the lower +75°/0° interface. For the specimens tested at 45% and 40% severities, the peak load slightly decreased initially with minimal damage, followed by an apparent increase. Finally, it kept a rapid decrease with delamination growth when the number of cycles exceeded 10^5. The load increase may be a result of stress re-distribution during the migration event, which caused tested specimens to have a higher delamination resistance, thus it took more cycles to complete the whole migration. The resulting scatter between specimens tested at the same severity may be attributed to the structural differences from specimen to specimen.

Three fatigue interrupted tests were loaded at 40% severity and terminated when they had 10%, 25% and 30% stiffness losses, respectively. The post-mortem edge views of the specimens with 10% and 25% stiffness losses are shown in Fig. 6b and Fig. 6c, respectively. The edge views of the specimen with 30% stiffness loss are not given here because they feature very similar failure mechanisms to the specimen with 25% stiffness loss. In comparison of Fig. 3b and Figs. 6b-c, it can be summarised that the damage mechanism under fatigue loading was similar to the static case, e.g. ply splits occurring in the lower -75° and +75° ply blocks and induced delaminations along the lower -75°/+75° and +75°/0° interfaces. This conclusion can also be confirmed by the CT results in Figs. 7-8. For the fatigue interrupted test 1, although stiffness loss was slow and small, delamination had migrated through the lower -75° and +75° ply block and induced a new delamination along the lower +75°/0° interface for about 4mm, as shown in the rear view. Further loading from the end of

interrupted test 1 until the end of interrupted test 2 mainly caused delamination growth along the lower +75°/0° interface, as concluded by the comparison of Fig. 7 and Fig. 8. This also means that the rapid stiffness loss after 10^5 cycles was mainly caused by the delamination growing along the lower +75°/0° interface.

4.2 Static and fatigue tests for specimens with θ = 60°

4.2.1 Static results

Fig. 9a shows a representative load versus displacement curve recorded during the single-step tests for specimens with θ = 60°. The load versus displacement curves of three interrupted tests are presented in Fig. 9b. The three interrupted specimens were loaded until reaching the three points as marked with red-colored circle in the Fig. 9a, respectively. Four main stages can be concluded, as indicated in Fig. 9a. In stage I, the load increased linearly with displacement until the initial damage. With further loading in stage II, ply splits initiated in the lower -60° ply block; delamination began to propagate inside the lower -60° ply block and migrated downwards along the lower -60°/+60° interface, as seen from the front view of the interrupted test 1 in Fig. 10. This is consistent with the X-ray CT results in Fig. 11. As shown in Fig. 11, small amount of delamination along the lower -60°/+60° interface occurred at the front edge, while no delamination was observed along the central +60°/-60° interface. Stiffness loss was minimal in this stage. Subsequently, the load showed a slow increase with further displacement. At the end of stage II, delaminations along the central +60°/-60° , lower -60°/+60° and lower +60°/0° interfaces grew significantly, as can be seen from the X-ray CT results of the interrupted test 2 in Fig. 12. In addition, ply splits started to occur in the lower -60° ply block at the rear edge. Different from the big load drop observed in the θ = 75° case, a small load drop happened at the end of stage II for the θ = 60° case. Delamination along the lower +60°/0° interface was delayed, with only small amount of delamination, as shown in Fig. 12, which can explain the small load drop at the end of stage II. In stage III, load recovered increasing from the small drop and more ply splits developed in the lower -60° and +60° ply blocks, as shown in Fig

13. However, further delamination growth along the central +60°/-60°, lower -60°/+60° and lower +60°/0° interfaces in this stage was not significant, from the comparison between Fig. 12 and Fig. 13. At the end of stage III, a big load drop occured, accompanied with rapid delamination migration towards the lower +60°/0° interface. The load drop was dramatic because ply splits induced delamination was finally connected and there was large amount of delamination along the lower +60°/0° interface. In stage IV, delamination kept growing in the lower +60°/0° interface because the zero degree ply suppressed further migration. The typical X-ray CT results of a $\theta = 60°$ specimen tested statically to full failure are shown in Fig. 14, the larger delamination area in the lower -60°/+60° interface and more ply splits in the lower -60° and +60° ply blocks implies a relatively more progressive delamination process in specimens with the $\theta = 60°$ case, in comparison to the $\theta = 75°$ case. In addition, delamination presented at the same in-plane position in the lower -60°/+60° and +60°/0° interfaces, as marked by five-pointed star in Fig. 14. This means these two delamination events simultaneously happened.

4.2.2 Fatigue results

For the $\theta = 60°$ case, the averaged displacement corresponding to 5% increase of compliance in the static load vs. displacement curve is 7.5mm. Three specimens were tested at both 40% and 45% severities, and a single specimen at 50% severity. Fig. 15 shows the fatigue results for all the cases, where the normalised maximum load curve underwent similar trends. The normalised maximum load firstly had a decrease due to small scale damage, followed by an obvious increase. Even at the high severity of 50%, the normalised maximum load curve had a similar increase before the final dramatic drop. The intermediate increase in stiffness indicated a higher resistance to the migration than initial stage. At the same severity 45%, fatigue loading on the three specimens was terminated after different cycles. The edge views were taken when the tests were paused and shown in Fig. 15. From this figure, it can be seen that the fatigue damage sequences before the second migration event were basically similar to the static case. The typical X-ray CT results of the fatigue

interrupted test 3 are shown in Fig. 16. In comparison between Fig. 13 and Fig. 15, no significant distinction existed for the damage status, between the static and fatigue cases.

5. Comparative analysis and summary

5.1 Static and fatigue ELS

The fracture surfaces between static and fatigue tests are macroscopically similar for specimens with $\theta = 75°$, as sketched in Fig. 17a. X_1 and X_2 in Fig. 17a indicate horizontal distances of migration points from the front of the PTFE insert, through the lower $-\theta_2$ and $+\theta_2$ ply block, respectively. These two parameters are introduced to quantitatively analyse the fracture surfaces. The detailed values of X_1 and X_2, their average values and standard deviations are listed in Table 2. For the $\theta = 60°$ case, the failure fracture surface between static and fatigue tests are different, as illustrated in Figs. 18a and b. In the fatigue specimen, the delamination along the -60°/+60° interface migrated downwards through the lower +60° ply block earlier (with lower value of X_2) and following delamination kept along the lower +60°/0° interface. In the static specimen, migration also occurred and resulted in delamination along the lower +60°/0° interface. However, the original delamination along the -60°/+60° interface grew forward at the same time. There were two delamination events co-existing in the static specimen, which was confirmed by the X-ray CT results. As shown in Table 2, the average values of X_1 and X_2 for static specimens were slightly higher than under fatigue loading, apart from the value of X_1 for $\theta = 60°$ case. This may indicate a greater propensity for migration under fatigue loading, which was also a conclusion in the mode I case [35].

The migration angles Ω_1 and Ω_2 marked in Fig. 17b are taken on the front sides of specimens via microscopic observation. A plot of the migration angles Ω_1 and Ω_2 is shown in Fig. 19. All data points are average values calculated from tested specimens. It can be seen that the values of Ω_1 and Ω_2 for static specimens are slightly lower than fatigue ones for all cases. Corresponding data from the previous DCB tests [35] are also included in the figure and further discussion follows later in

the next section.

Migration details became apparent after exposing the specimen fracture surfaces. Thus, fractographic analysis was implemented using SEM in an attempt to correlate the macroscopic observation of the delamination migration behaviour with the microscopic fracture mechanism. Figs. 20-21 show the images of the lower fracture surface from typical static specimens with $\theta = 75°$ and 60°, respectively. Figs. 22-23 correspond to the fatigue case. One macro picture of fracture surface is firstly shown in the topleft subplot of each figure, followed by SEM images taken from positions indicated in the macro picture. Dense distribution of micro cracks, taking the form of shear cusps, was observed at the surface in all figures. Delamination growth exhibits inherent directionality, which preferably grew parallel to either the lowermost or the uppermost fibre direction at a ply interface [42]. It is assumed that the initiation and growth of micro cracks decreased the loading capacity of epoxy matrix at the micro scale, resulting in the decrease of in-plane shear stress at ply level. Most shear cusps were not strictly perpendicular to the fibres, but with a slight angle. This means the continued propagation was in a mode II dominated mixed mode. Their size varied considerably, possibly controlled by the volume fraction of the matrix confined by fibres.

In general, the morphologies of facture surfaces under static and fatigue loading were very similar. Thus further descriptions on the SEM images are only made for the static cases. As shown in Figs. 20b and 20c, many ply splits occurred at the surrounding area of the insert front. The central delamination propagated along the lower -75° fibre direction and towards the side of the specimen, which can be seen from the orientation of shear cusps in this area. This agrees with the results obtained by X-ray CT. It was observed that a large amount of matrix was still adhered to fibres on the fracture surfaces in Fig. 20c. This indicates a strong bond between fibres and the surrounding matrix at this location [43]. In Fig. 20d, delamination in the lower -75°/+75° interface presented a matrix-dominated fracture surface featured with imprints of -75° fibres, which indicates a transition of the propagating delamination away from the -75° fibres. Delamination gradually

kinked to the adjacent lower +75° ply block (Fig. 20e) and exposed +75° fibres were observed. It finally migrated through the lower +75° ply block towards the lower +75°/0° interface, resulting in obvious migration line across the entire specimen width. In Figs. 20e and 20f, clear fibres exposed under shear loading due to lower shear strength of fibre/matrix interface than the matrix.

When the value of θ decreases from 75° to 60°, the triangle area (as sketched in Fig. 17a) also changed. As shown in Fig. 21, the microscopic features were similar with those of the specimen with θ = 75°. In Fig. 21d, the tendency to migrate through the lower +60° ply block is clear, which can be concluded from the existing ply splits aligned with the +60° fibre direction. Delamination in the lower -60°/+60° interface gradually transited from interfacially adjacent to -60° ply (with exposed -60° fibres) to interfacially adjacent to +60° ply (with exposed +60° fibres), as shown in Fig. 21e.

5. 2 Mode I and II

The macro fracture surfaces under mode I and II loading are similar for specimens with θ = 75°, as sketched in Fig. 17a. However, obvious differences exist between macro characteristics of fracture surfaces for specimens with θ = 60°, as summarised in Fig. 24. In the DCB specimens, the extent of ply delving into the bounding ply varies across the width of the specimen and a rough surface is shown, but the surface of ELS specimens has a relatively clean appearance. Similarly, the sequence of damage events and migration mechanisms are basically same in both DCB and ELS specimens with θ = 75°. While it is not the case for static specimens with θ = 60°, the main differences lie in the double-delamination events, as compared in Fig. 25.

The average values of X_1 and X_2 from DCB [35] and ELS specimens are summarised in Table 3. It can be seen that the values of X_1 and X_2 under mode I loading are higher than these of mode II case, for both stacking sequences. In the DCB specimens, many ply delving [32] and resulted fibre bridging were observed, which caused additional resistance to the delamination growth. However, there seems to be no ply delving and bridging fibres in the ELS specimens. It is expected that fibre

bridging prevented the delamination from kinking through ply blocks, thus essentially delaying the location at which migration occurs. The propagating delamination will meander around the interface [32] with increasing tortuosity of the crack path. This may partly explain why the values of X_1 and X_2 of the DCB specimens are higher than those of ELS specimens.

The migration angles Ω_1 and Ω_2 for the DCB and ELS specimens are compared in Fig. 19. Overall, the values of Ω_1 and Ω_2 for static specimens are slightly lower than fatigue ones. In addition, the value of Ω_1 seems to be independent of loading modes and θ; it is around 50° and 56° in static and fatigue specimens, respectively. The loading modes and θ have a mild effect on the value of Ω_2 (varying between 36° and 56°) while further firm conclusions cannot be drawn from the present observations alone, meaning that more experimental data are required in the future.

6 Conclusions

Delamination migration is an important mechanism in multidirectional composite laminates, where the tortuosity of the crack path can delay delamination propagation. Experimental studies on delamination migration were conducted under mode II loading and a comparative analysis was done with previous test results from mode I cases. The damage sequences under mode I and II loading were similar for specimens with $\theta = 75°$, while those were different for the $\theta = 60°$ case. In the latter case, two delamination events co-existed in the static ELS specimens. All the specimens under both static and fatigue loading had fairly similar migration mechanisms, with ply splits developing inside the specimens and finally resulting in delamination migration. The presence of these ply splits promoted the delamination to migrate such that the induced delamination found an ideal path with the lowest fracture resistance. The migration process in the DCB specimens was relatively more stable than in the ELS specimens. Detailed examination of the migration process via X-ray CT and optical inspection revealed that extension of ply splits will follow the fibre direction. The ply splits occurred through the non-zero plies, increasing the delamination resistance and a wavy appearance of the fracture surface in the DCB specimens, while there was a relatively smooth appearance in the

ELS specimens. For all specimens, SEM images showed that fibre imprints and cusps were two dominant micro-features on the failed fracture surfaces. Generally, the value of first migration angle Ω_1 seems to be independent of loading mode and stacking sequence; it was around 50° and 56° in static and fatigue specimens, respectively. However, the values of Ω_2 vary between 36° and 56° in different specimens. Considering the high repeatability of the tests, the experimental results presented here can used as validation data for modeling methods aimed at simulating delamination migration.

Acknowledgement

The authors would like to thank Mike I. Jones and Rico Kuehlewind for their technical support and advice. The work of Yu Gong is financially supported by the China Scholarship Council (CSC) and the Fundamental Research Funds for the Central Universities.

References

[1] Greenhalgh ES, Rogers C, Robinson P. Fractographic observations of delamination growth mechanism. 16th International Conference on Composite Materials, Japan, 2007.
[2] Gong Y, Zhao L, Zhang J, Wang Y, Hu N. Delamination propagation criterion including the effect of fiber bridging for mixed-mode I/II delamination in CFRP multidirectional laminates. Compos Sci Technol 2017; 151: 302-9.
[3] Zhao L, Gong Y, Qin T, Mehmood S, Zhang J. Failure prediction of out-of-plane woven composite joints using cohesive element. Compos Struct 2013; 106: 407-16.
[4] Gong Y, Zhao L, Zhang J, Hu N. An improved power law criterion for the delamination propagation with the effect of large-scale fiber bridging in composite multidirectional laminates. Compos Struct 2018; 184: 961-8.
[5] Zhao L, Wang Y, Zhang J, Gong Y, Lu Z, Hu N, Xu J. An interface-dependent model of plateau fracture toughness in multidirectional CFRP laminates under mode I loading. Composites Part B: Engineering 2017; 131: 196-208.
[6] Zhao L, Wang Y, Zhang J, Gong Y, Hu N, Li N. XFEM-based model for simulating zigzag delamination growth in laminated composites under mode I loading. Compos Struct 2017; 160: 1155-62.
[7] Canturri C, Greenhalgh ES, Pinho ST, Ankersen J. Delamination growth directionality and the subsequent migration processes-The key to damage tolerant design. Compos A Appl Sci Manuf 2013; 54: 79-87.
[8] Krueger R, Cvitkovich MK, O'Brien TK, Minguet PJ. Testing and analysis of composite skin/stringer debonding under multi-axial loading. J Compos Mater 2000; 34(15): 1263-300.
[9] Hull D, Shi YB. Damage mechanism characterization in composite damage tolerance investigations. Compos Struct 1993; 23(2): 99-120.
[10] Greenhalgh E, Singh S. Investigation of the failure mechanisms for delamination growth from embedded defects. Proceedings of the 12th International Conference on Composite Materials, Paris (France), 1999.
[11] Canturri C, Greenhalgh ES, Pinho ST, Nilsson S. Delamination growth mechanism from

embedded defects in compression. Proceedings of ICCM18, Jeju Island, 2011.
[12] Hallett SR, Green BG, Jiang WG, Wisnom MR. An experimental and numerical investigation into the damage mechanisms in notched composites. Compos A Appl Sci Manuf 2009; 40(5): 613-24.
[13] Tao J, Sun CT. Influence of ply orientation on delamination in composite laminates. J Compos Mater 1998; 32(21): 1933-47.
[14] Zhao L, Gong Y, Zhang J, Wang Y, Lu Z, Peng L, Hu N. A novel interpretation of fatigue delamination growth behavior in CFRP multidirectional laminates. Compos Sci Technol 2016; 133: 79-88.
[15] Peng L, Zhang J, Zhao L, Bao R, Yang H, Fei B. Mode I delamination growth of multidirectional composite laminates under fatigue loading. J Compos Mater 2011; 45(10): 1077-90.
[16] Zhang J, Peng L, Zhao L, Fei B. Fatigue delamination growth rates and thresholds of composite laminates under mixed mode loading. Int J Fatigue 2012; 40: 7-15.
[17] Peng L, Xu J, Zhang J, Zhao L. Mixed mode delamination growth of multidirectional composite laminates under fatigue loading. Eng Fract Mech 2012; 96: 676-86.
[18] Samborski S. Analysis of the end-notched flexure test configuration applicability for mechanically coupled fiber reinforced composite laminates. Compos Struct 2017; 163: 342-9.
[19] Samborski S. Prediction of delamination front's advancement direction in the CFRP laminates with mechanical couplings subjected to different fracture toughness tests. Compos Struct 2018: In Press.
[20] Samborski S. Numerical analysis of the DCB test configuration applicability to mechanically coupled Fiber Reinforced Laminated Composite beams. Compos Struct 2016; 152: 477-87.
[21] Turon A, Camanho PP, Costa J, Renart J. Accurate simulation of delamination growth under mixed-mode loading using cohesive elements: definition of interlaminar strengths and elastic stiffness. Compos Struct 2010; 92(8): 1857-64.
[22] May M, Hallett SR. A combined model for initiation and propagation of damage under fatigue loading for cohesive interface elements. Compos A Appl Sci Manuf 2010; 41(12): 1787-96.
[23] Belytschko T, Gracie R, Ventura G. A review of extended/generalized finite element methods for material modeling. Model Simul Mater Sc 2009; 17(4): 43001.
[24] Higuchi R, Okabe T, Nagashima T. Numerical simulation of progressive damage and failure in composite laminates using XFEM/CZM coupled approach. Compos A Appl Sci Manuf 2017; 95: 197-207.
[25] Abdullah NA, Curiel-Sosa JL, Taylor ZA, Tafazzolimoghaddam B, Martinez Vicente JL, Zhang C. Transversal crack and delamination of laminates using XFEM. Compos Struct 2017; 173: 78-85.
[26] Ling D, Yang Q, Cox B. An augmented finite element method for modeling arbitrary discontinuities in composite materials. Int J Fracture 2009; 156(1): 53-73.
[27] Chen BY, Tay TE, Pinho ST, Tan VBC. Modelling delamination migration in angle-ply laminates. Compos Sci Technol 2017; 142: 145-55.
[28] Ratcliffe JG, Czabaj MW, O'Brien TK. A Test for Characterizing Delamination Migration in Carbon/Epoxy Tape Laminates. NASA/TM-2013-218028, 2013.
[29] De Carvalho NV, Chen BY, Pinho ST, Ratcliffe JG, Baiz PM, Tay TE. Modeling delamination migration in cross-ply tape laminates. Compos A Appl Sci Manuf 2015; 71: 192-203.
[30] Zhao L, Zhi J, Zhang J, Liu Z, Hu N. XFEM simulation of delamination in composite laminates. Compos A Appl Sci Manuf 2016; 80: 61-71.
[31] Li X, Chen J. An extended cohesive damage model for simulating multicrack propagation in fibre composites. Compos Struct 2016; 143: 1-8.
[32] Ratcliffe JG, DeCarvalho NV. Investigating delamination migration in composite tape laminates. NASA/TM-2014-218289, 2014.

[33] Pernice MF, De Carvalho NV, Ratcliffe JG, Hallett SR. Experimental study on delamination migration in composite laminates. Compos A Appl Sci Manuf 2015; 73: 20-34.
[34] Canturri C, Greenhalgh ES, Pinho ST. The relationship between mixed-mode II/III delamination and delamination migration in composite laminates. Compos Sci Technol 2014; 105: 102-9.
[35] Gong Y, Zhang B, Hallett SR. Delamination migration in multidirectional composite laminates under mode I quasi-static and fatigue loading. Compos Struct 2018; 189: 160-76.
[36] Refahi Oskouei A, Zucchelli A, Ahmadi M, Minak G. An integrated approach based on acoustic emission and mechanical information to evaluate the delamination fracture toughness at mode I in composite laminate. Mater Design 2011; 32(3): 1444-55.
[37] Zhao L, Gong Y, Zhang J, Chen Y, Fei B. Simulation of delamination growth in multidirectional laminates under mode I and mixed mode I/II loadings using cohesive elements. Compos Struct 2014; 116: 509-22.
[38] Davidson BD, Krüger R, König M. Three-dimensional analysis of center-delaminated unidirectional and multidirectional single-leg bending specimens. Compos Sci Technol 1995; 54(4): 385-94.
[39] Davidson BD, Kruger R, König M. Three dimensional analysis and resulting design recommendations for unidirectional and multidirectional end-notched flexure tests. J Compos Mater 1995; 29(16): 2108-33.
[40] ISO/DIS 15114, Fibre-reinforced plastic composites-Determination of the mode II fracture resistance for unidirectionally reinforced materials using the calibrated end-loaded split (C-ELS) test and an effective crack length approach, 2014.
[41] Brunner AJ, Blackman B, Davies P. A status report on delamination resistance testing of polymer-matrix composites. Eng Fract Mech 2008; 75(9): 2779-94.
[42] Greenhalgh ES, Rogers C, Robinson P. Fractographic observations on delamination growth and the subsequent migration through the laminate. Compos Sci Technol 2009; 69(14): 2345-51.
[43] Charalambous G, Allegri G, Hallett SR. Temperature effects on mixed mode I/II delamination under quasi-static and fatigue loading of a carbon/epoxy composite. Compos A Appl Sci Manuf 2015; 77: 75-86.

Figure Captions

Fig. 1. (a) Specimen configurations and (b) ELS test set-up (unit: mm).

Fig. 2. Typical load vs. displacement curve of the static ELS tests with $\theta = 75°$.

Fig. 3. (a) Load vs. displacement curves and (b) two-side edge views of the interrupted ELS tests with $\theta = 75°$; arrows indicate initial crack-tip locations with the minimum scale of 1 mm.

Fig. 4. CT observed damage of a $\theta = 75°$ specimen for the static interrupted test 1; dash line marks the location of pre-crack tip, which applies to all the following CT scan images. (The crack propagation direction is from left to right)

Fig. 5. CT observed damage of a $\theta = 75°$ specimen for the static interrupted test 2. (The crack propagation direction is from left to right)

Fig. 6. (a) Fatigue results of specimens with $\theta = 75°$ and (b-c) Edge views at different stiffness losses during fatigue tests; arrows mark the location of the initial crack tip; the minimum scale of the attached paper ruler is 1 mm.

Fig. 7. CT observed damage of a $\theta = 75°$ specimen for the fatigue interrupted test 1.

Fig. 8. CT observed damage of a $\theta = 75°$ specimen for the fatigue interrupted test 2.

Fig. 9. Load vs. displacement curves from (a) a specimens tested statically to full failure and (b) three interrupted specimens, with $\theta = 60°$.

Fig. 10. Edge views at key stages during the tests (arrows mark the location of the initial crack tip and the minimum scale visible is in mm).

Fig. 11. CT observed damage of a $\theta = 60°$ specimen for the static interrupted test 1.

Fig. 12. CT observed damage of a $\theta = 60°$ specimen for the static interrupted test 2.

Fig. 13. CT observed damage of a $\theta = 60°$ specimen for the static interrupted test 3.

Fig. 14. CT observed damage of a $\theta = 60°$ specimen tested statically to full failure.

Fig. 15. (a) Fatigue results obtained from the fatigue specimens with $\theta = 60°$ and (b) edge views at different stiffness losses during fatigue tests (arrows mark the location of the initial crack tip and the

minimum scale visible is 1 mm).

Fig. 16. CT observed damage of a θ = 60° specimen for the fatigue interrupted test 3.

Fig. 17. (a) 3D sketch of fracture surface of static and fatigue ELS specimens with θ = 75° (b) Delamination path.

Fig. 18. Sketch of fracture surface of (a) static (b) fatigue ELS specimen with θ = 60°.

Fig. 19. Migration angles of DCB and ELS static (S) and fatigue (F) specimens with θ = 75° and 60°.

Fig. 20. Micrographs at different locations on the fracture surface from a typical static specimen with θ = 75°.

Fig. 21. Micrographs at different locations on the fracture surface from a typical static specimen with θ = 60°.

Fig. 22. Micrographs at different locations on the fracture surface from a typical fatigue specimen with θ = 75°.

Fig. 23. Micrographs at different locations on the fracture surface from a typical fatigue specimen with θ = 60°.

Fig. 24. Summary of the failed fracture surfaces of static and fatigue DCB and ELS specimens with θ = 60°.

Fig. 25. Sketch of fracture surface from static (a) DCB and (b) ELS specimens with θ = 60°.

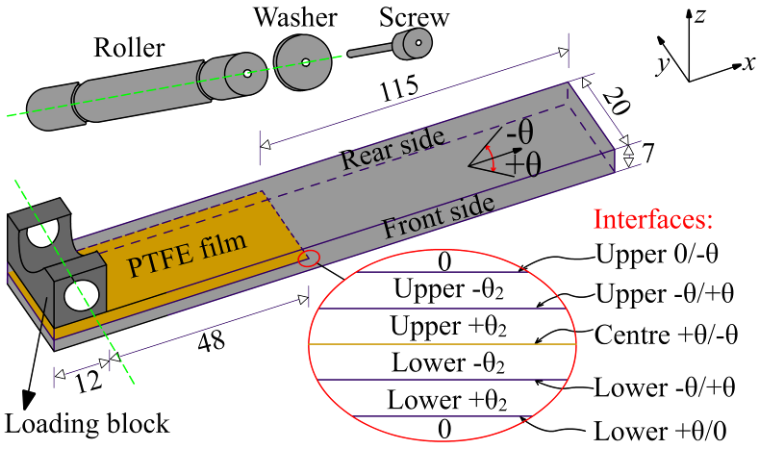

(a)

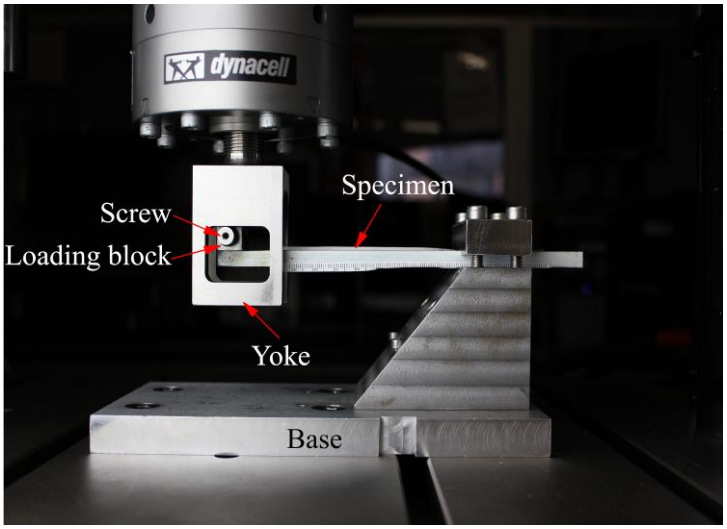

(b)

Fig. 1. (a) Specimen configurations and (b) ELS test set-up (unit: mm).

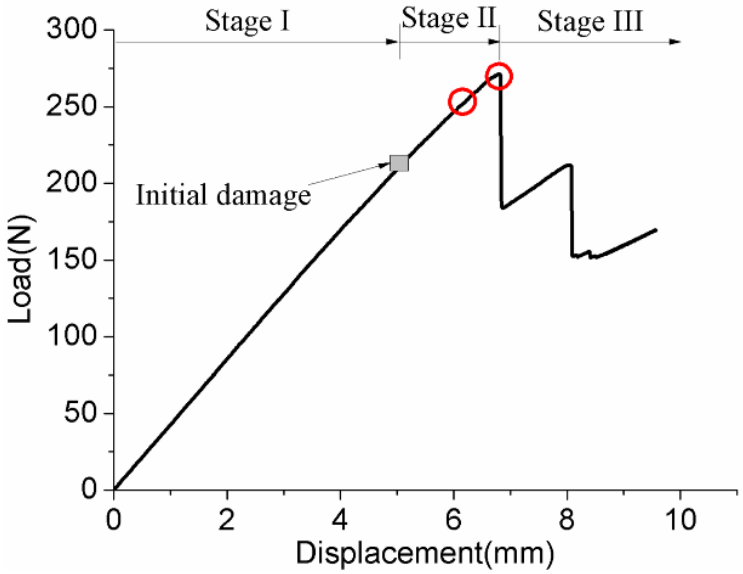

Fig. 2. Typical load vs. displacement curve of the static ELS tests with θ = 75°.

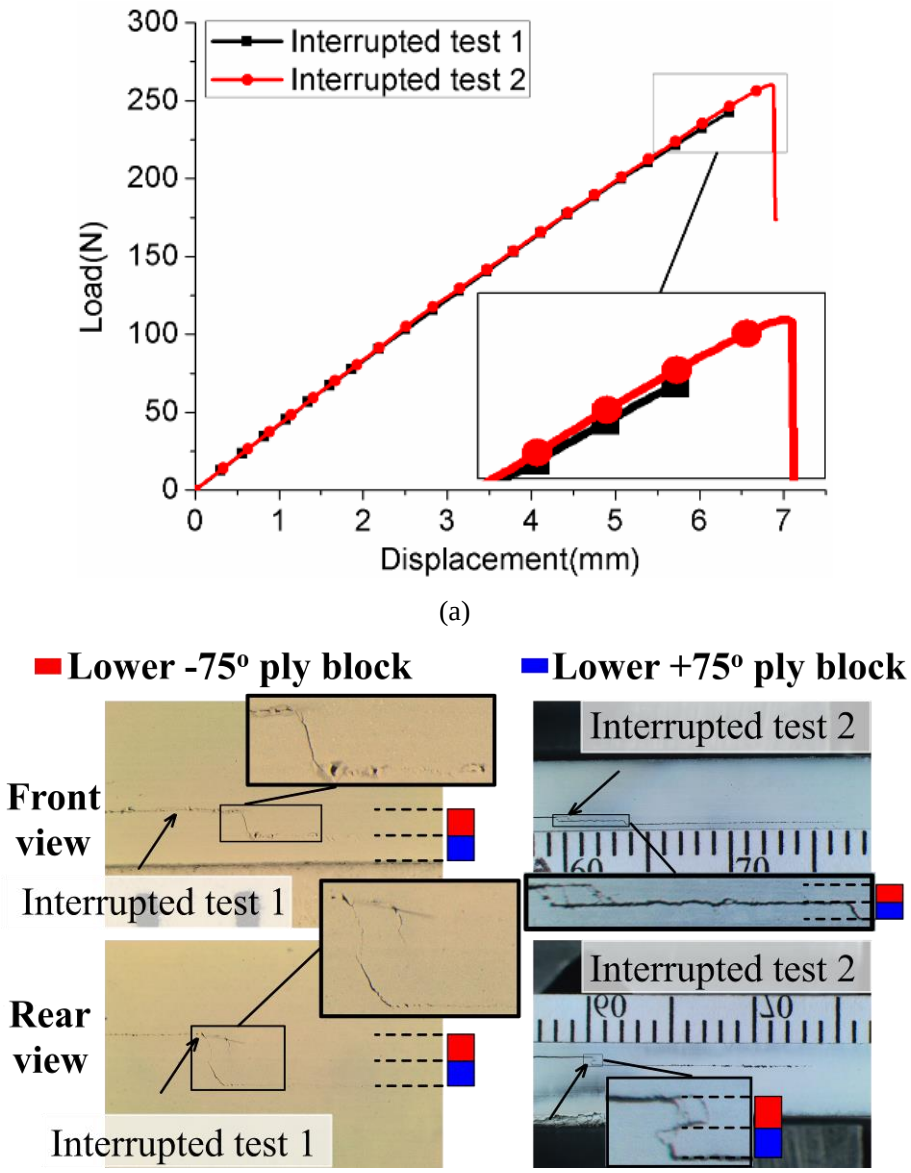

Fig. 3. (a) Load vs. displacement curves and (b) two-side edge views of the interrupted ELS tests with θ = 75°; arrows indicate initial crack-tip locations with the minimum scale of 1 mm.

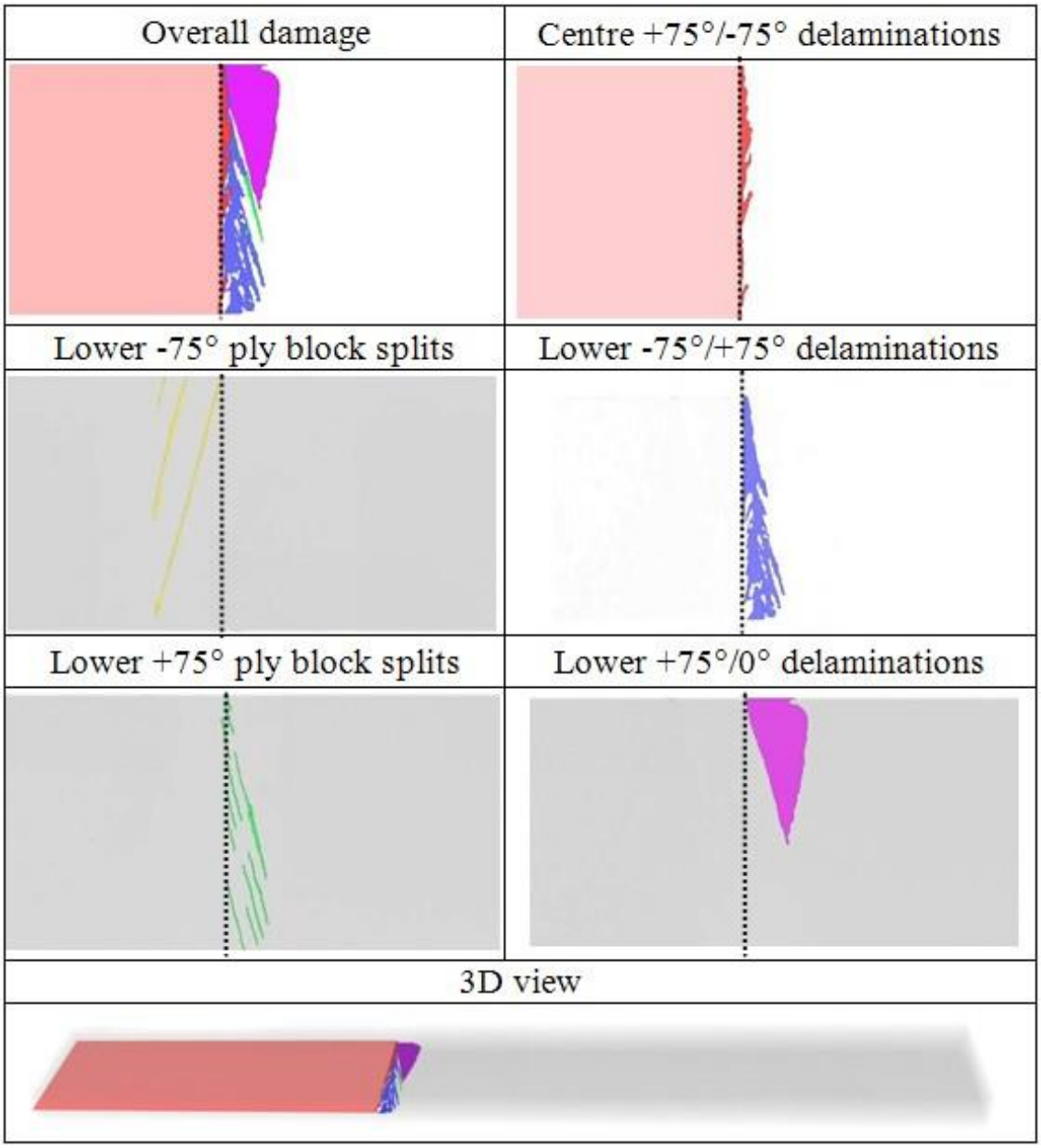

Fig. 4. CT observed damage of a θ = 75° specimen for the static interrupted test 1; dash line marks the location of pre-crack tip, which applies to all the following CT scan images. (The crack propagation direction is from left to right)

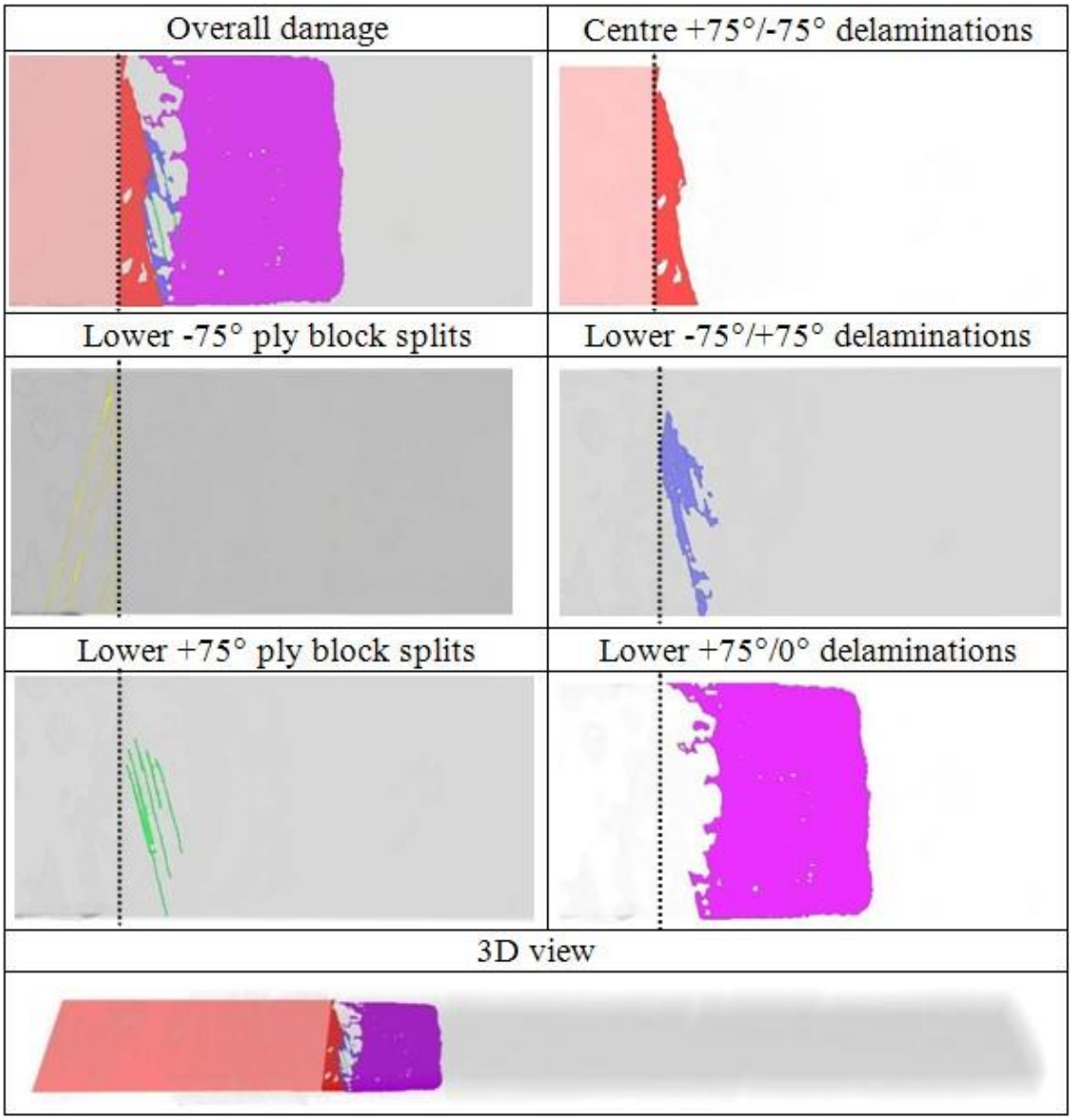

Fig. 5. CT observed damage of a θ = 75° specimen for the static interrupted test 2. (The crack propagation direction is from left to right)

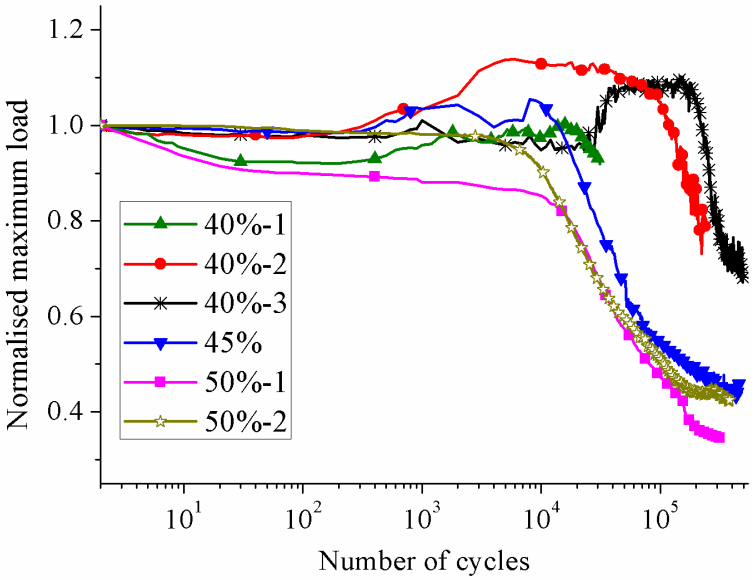

(a)

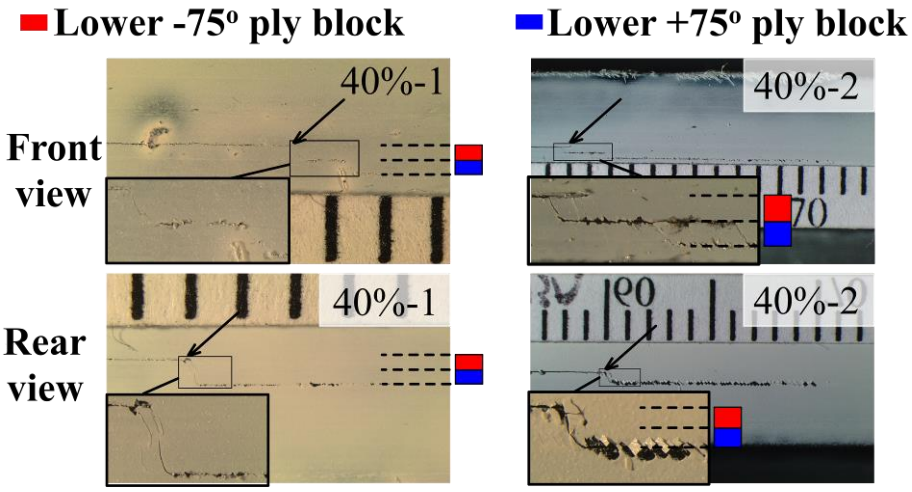

(b) (c)

Fig. 6. (a) Fatigue results of specimens with θ = 75° and (b-c) Edge views at different stiffness losses during fatigue tests; arrows mark the location of the initial crack tip; the minimum scale of the attached paper ruler is 1 mm.

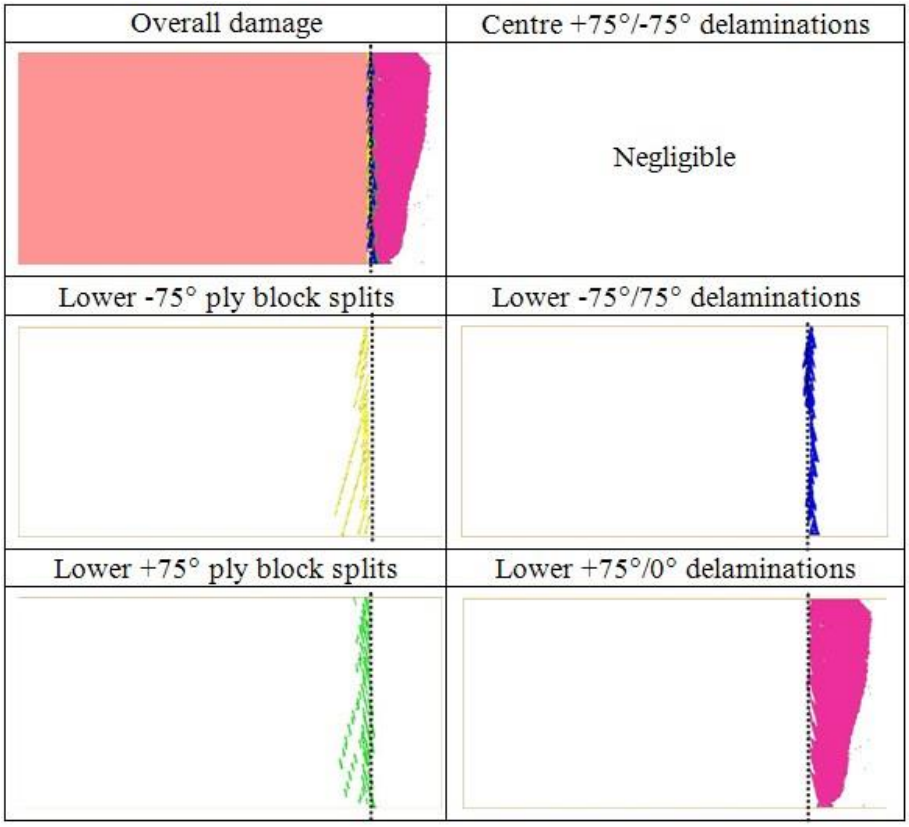

Fig. 7. CT observed damage of a θ = 75° specimen for the fatigue interrupted test 1.

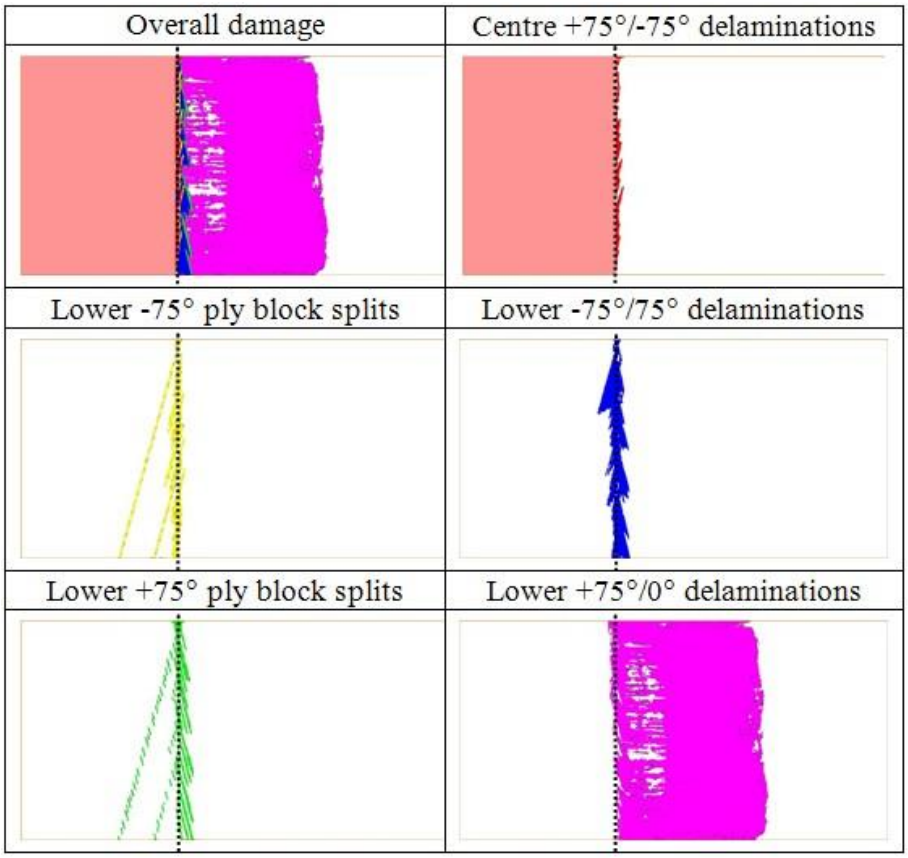

Fig. 8. CT observed damage of a θ = 75° specimen for the fatigue interrupted test 2.

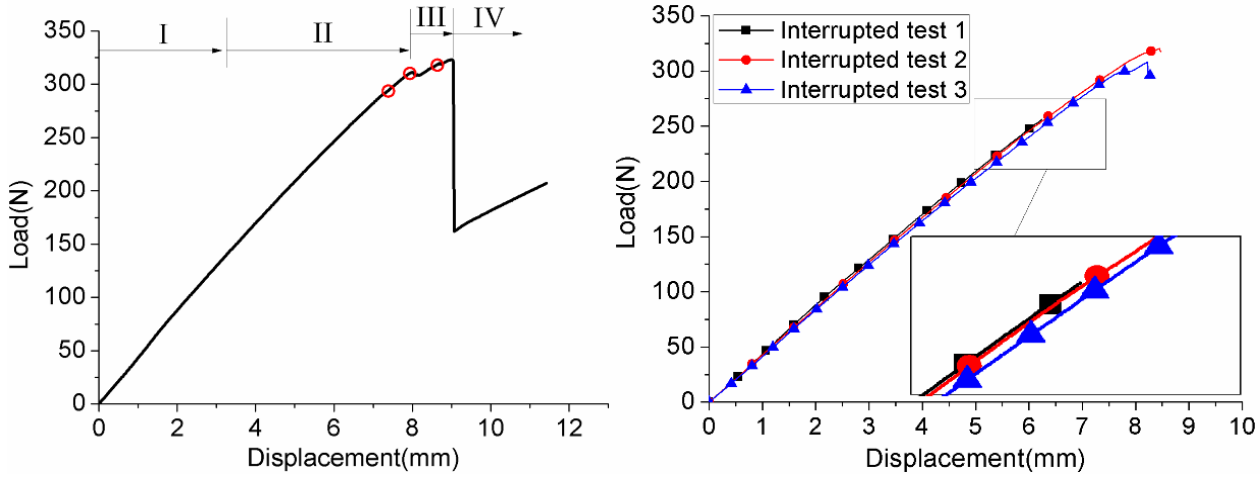

(a) (b)

Fig. 9. Load vs. displacement curves from (a) a specimens tested statically to full failure and (b) three interrupted specimens, with θ = 60°.

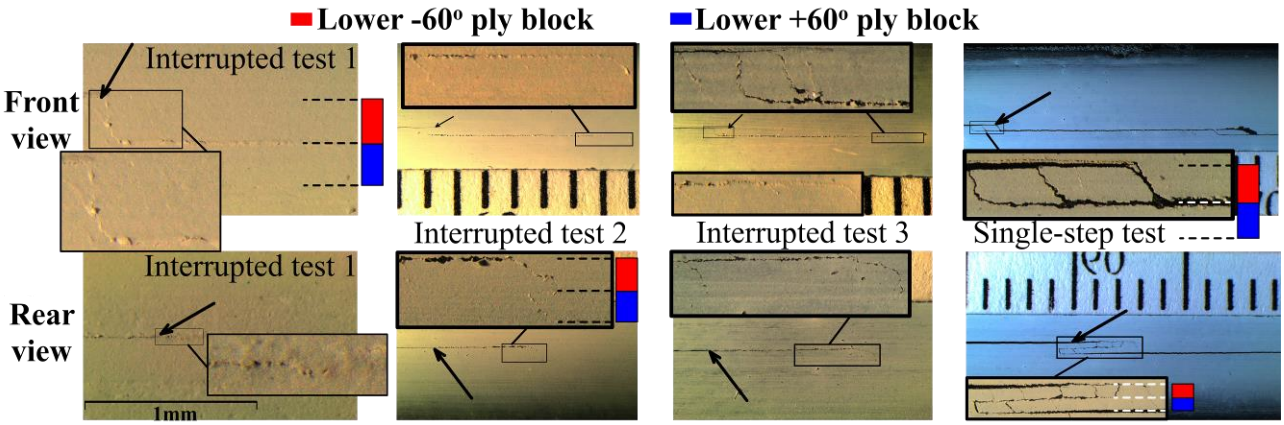

Fig. 10. Edge views at key stages during the tests (arrows mark the location of the initial crack tip and the minimum scale visible is in mm).

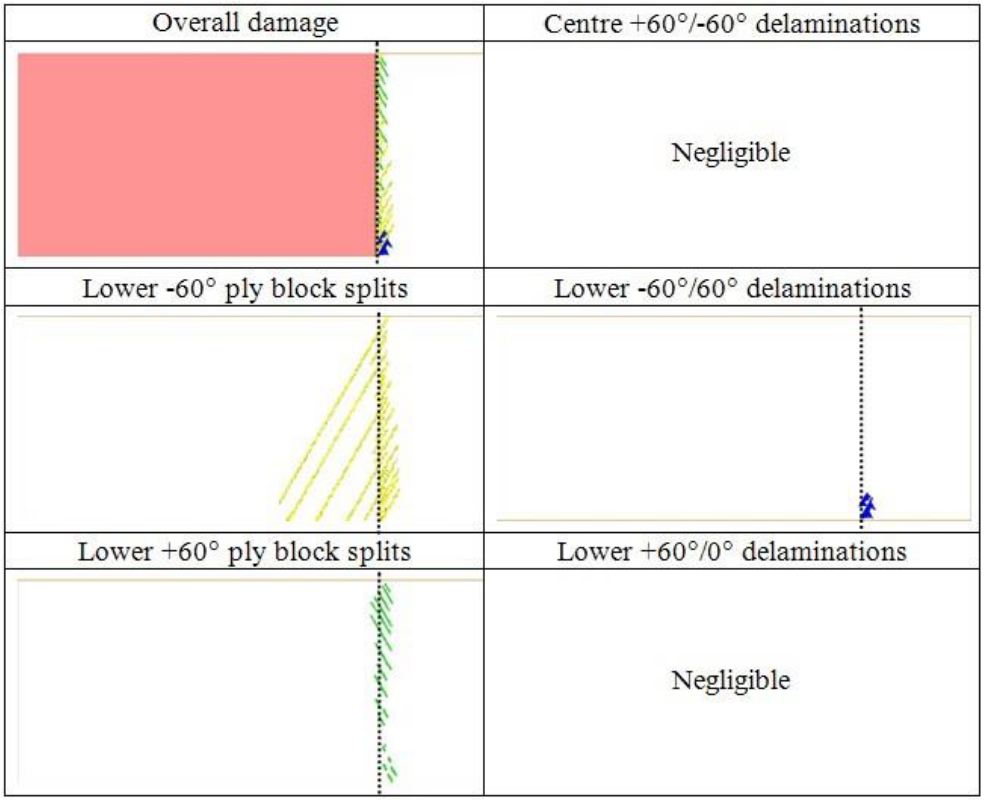

Fig. 11. CT observed damage of a θ = 60° specimen for the static interrupted test 1.

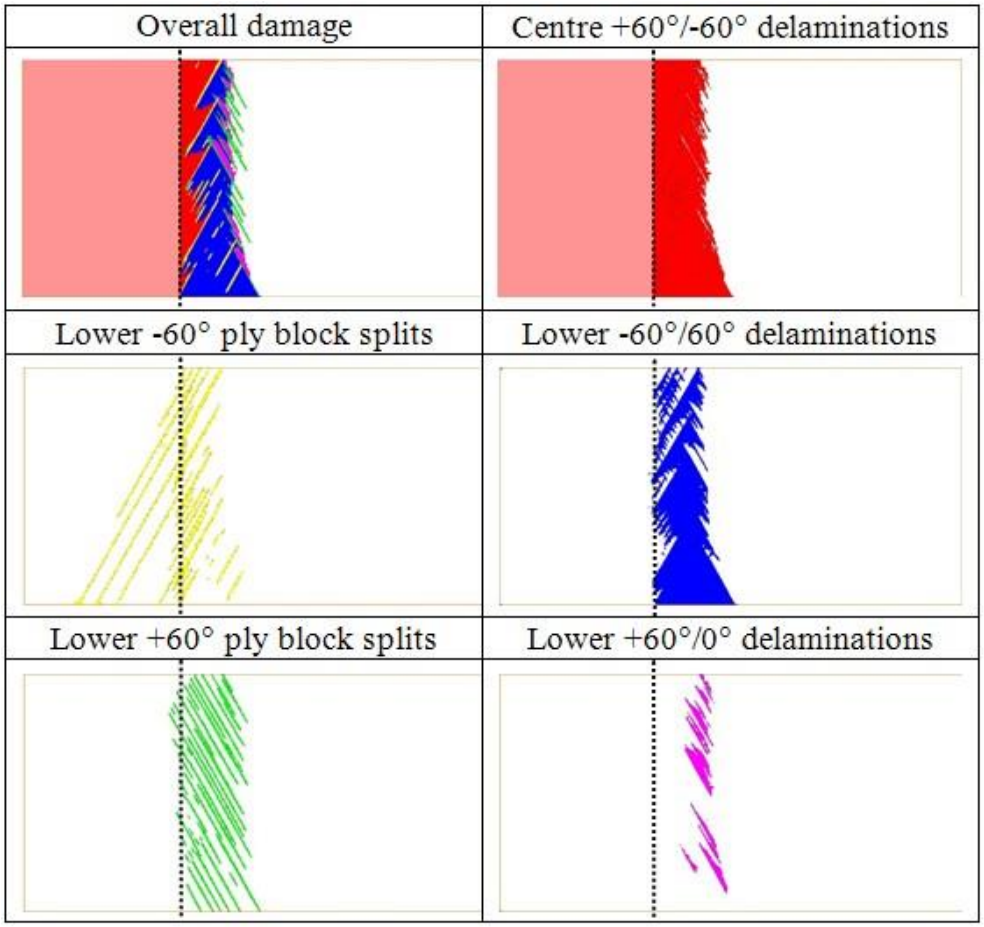

Fig. 12. CT observed damage of a θ = 60° specimen for the static interrupted test 2.

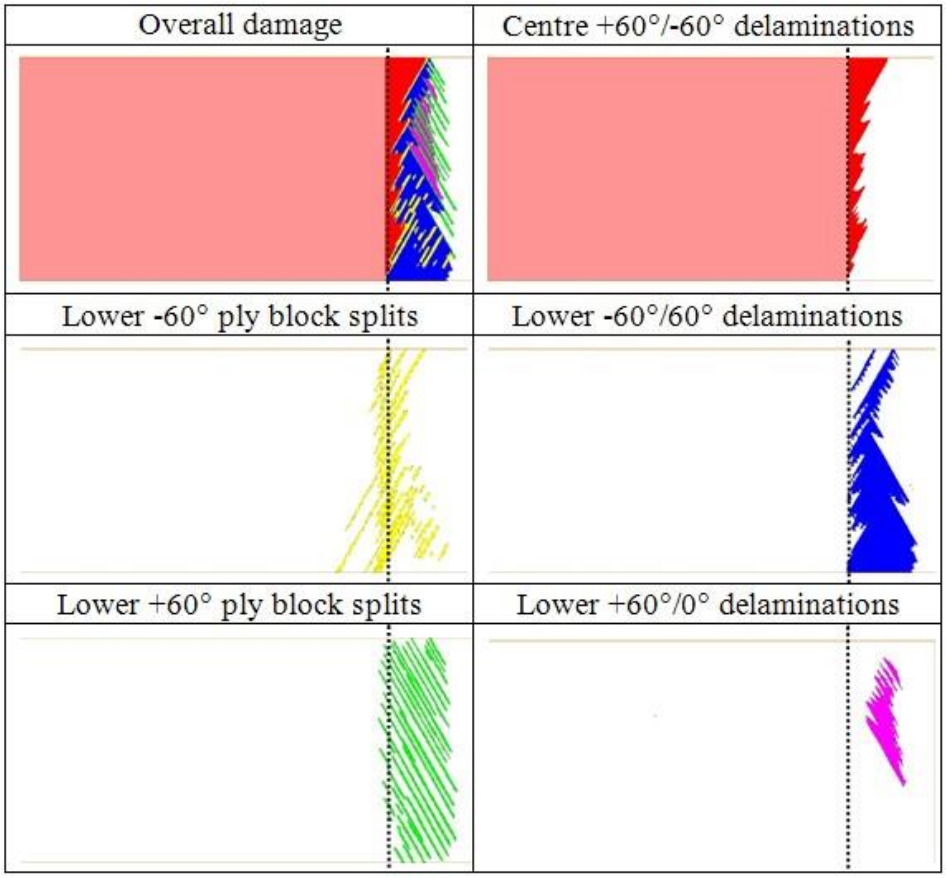

Fig. 13. CT observed damage of a θ = 60° specimen for the static interrupted test 3.

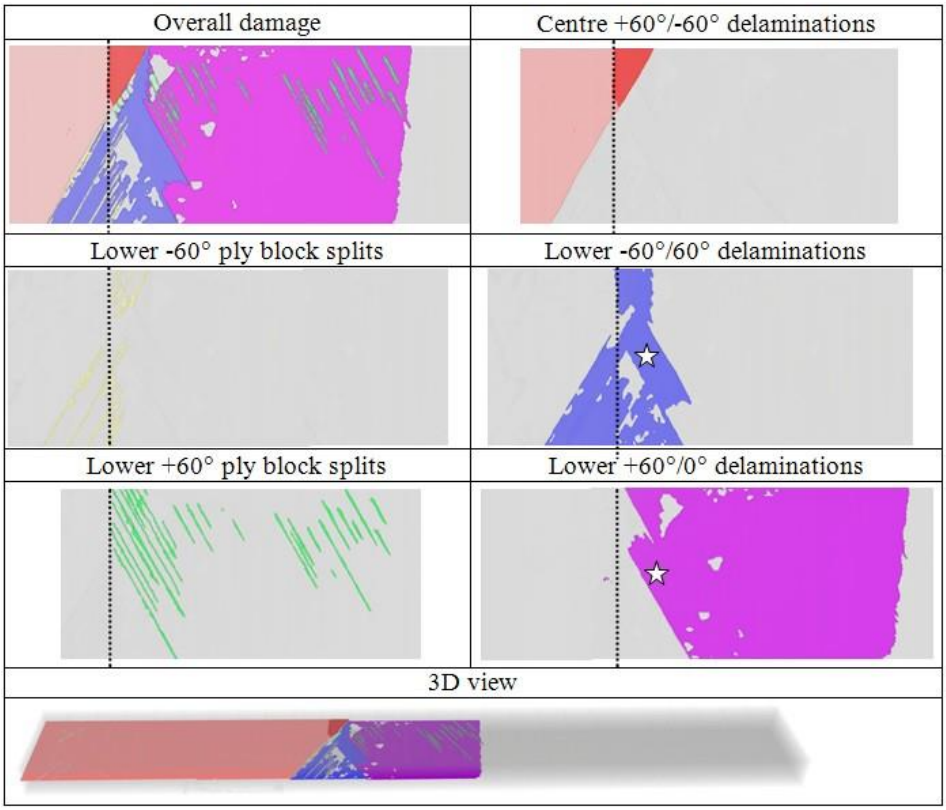

Fig. 14. CT observed damage of a θ = 60° specimen tested statically to full failure.

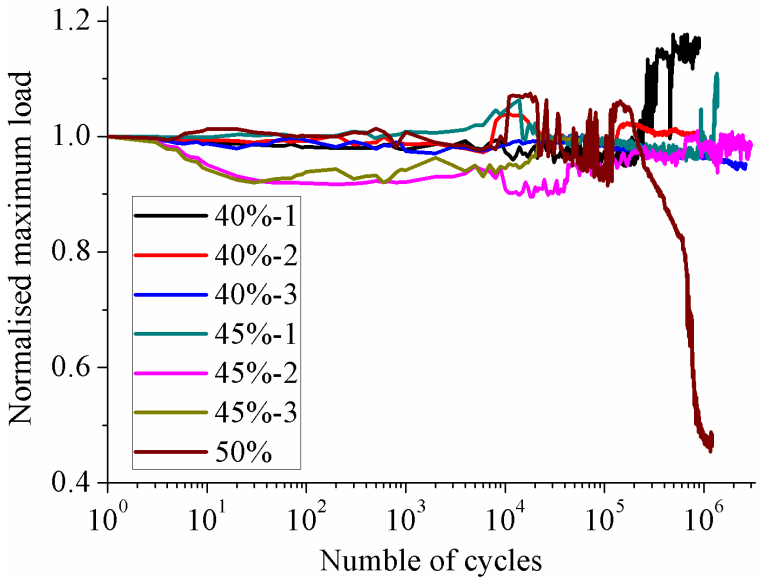

(a)

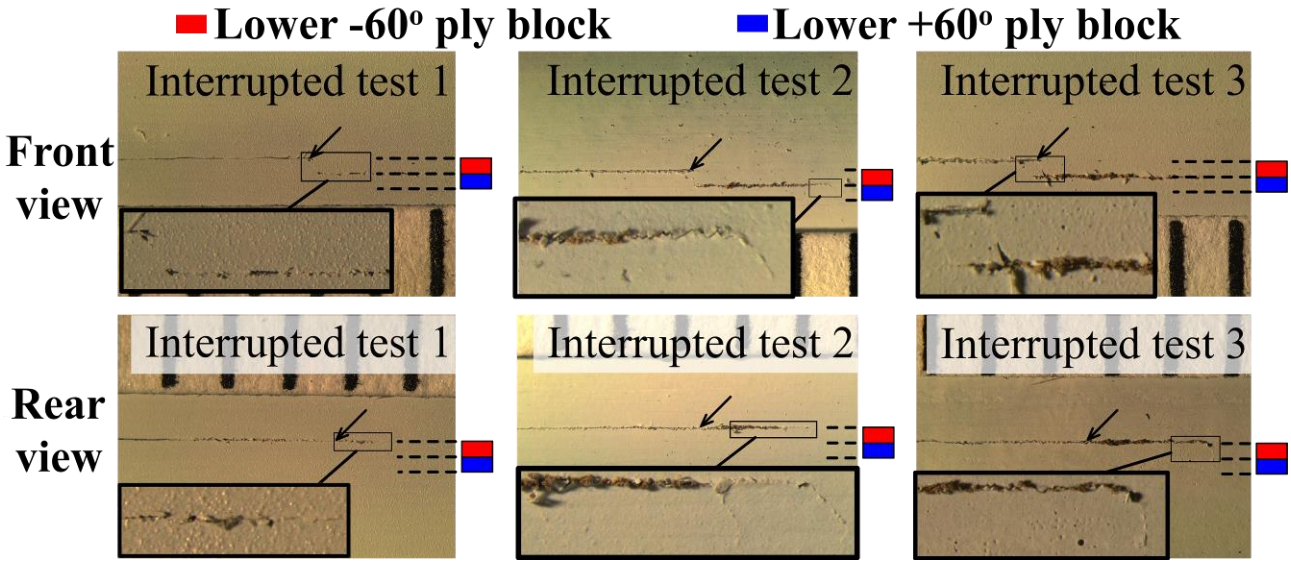

(b)

Fig. 15. (a) Fatigue results obtained from the fatigue specimens with θ = 60° and (b) edge views at different stiffness losses during fatigue tests (arrows mark the location of the initial crack tip and the minimum scale visible is 1 mm).

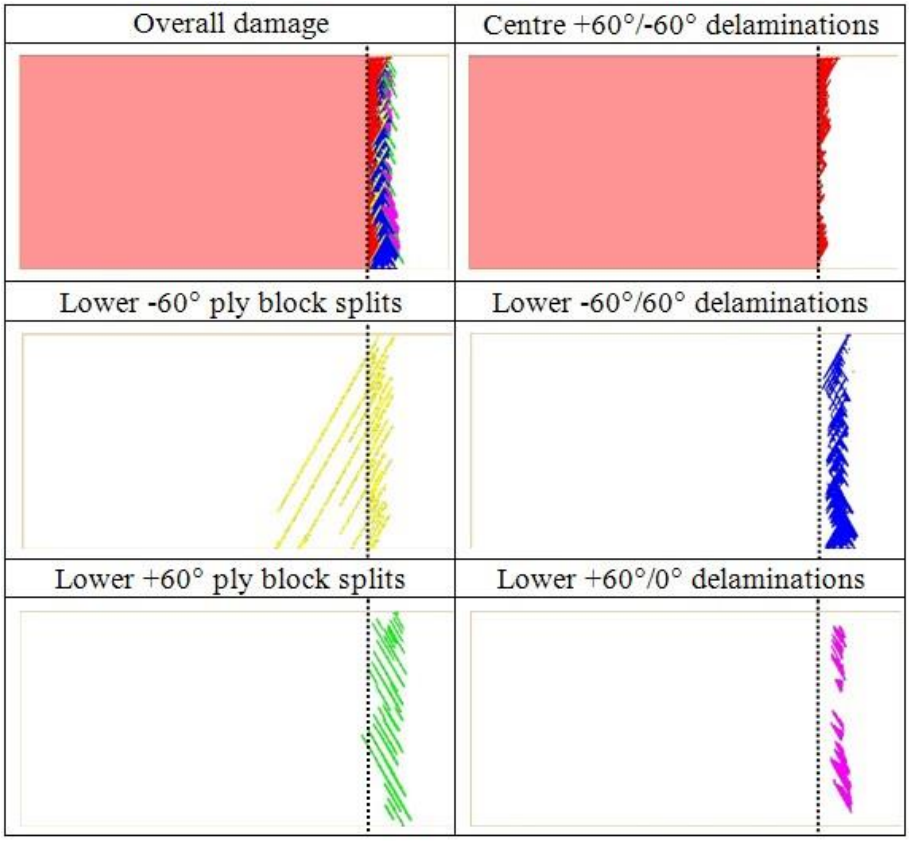

Fig. 16. CT observed damage of a θ = 60° specimen for the fatigue interrupted test 3.

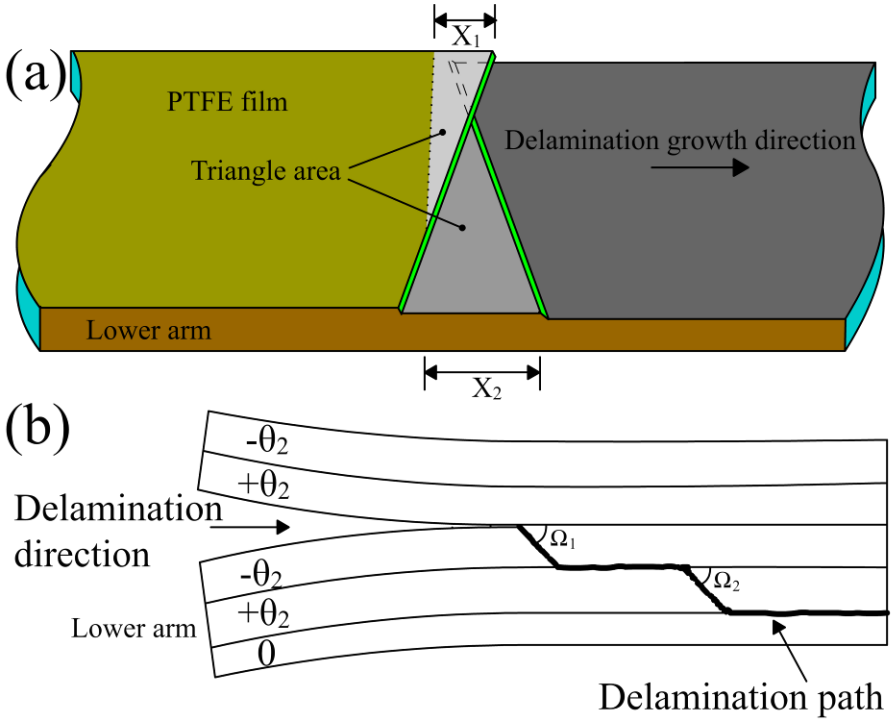

Fig. 17. (a) 3D sketch of fracture surface of static and fatigue ELS specimens with θ = 75° (b) Delamination path.

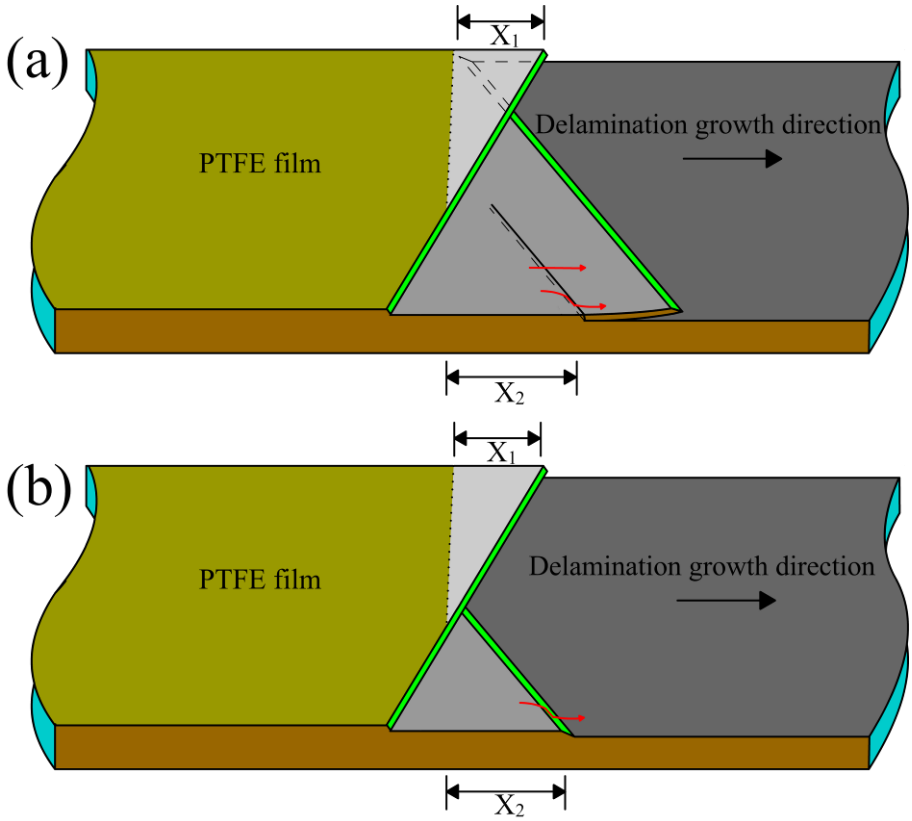

Fig. 18. Sketch of fracture surface of (a) static (b) fatigue ELS specimen with θ = 60°.

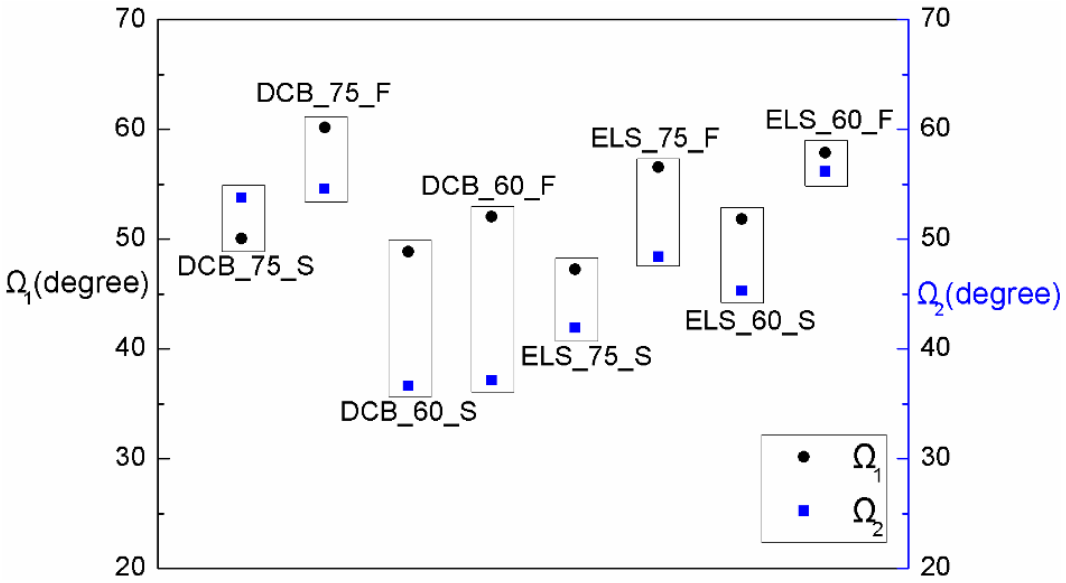

Fig. 19. Migration angles of DCB and ELS static (S) and fatigue (F) specimens with θ = 75° and 60°.

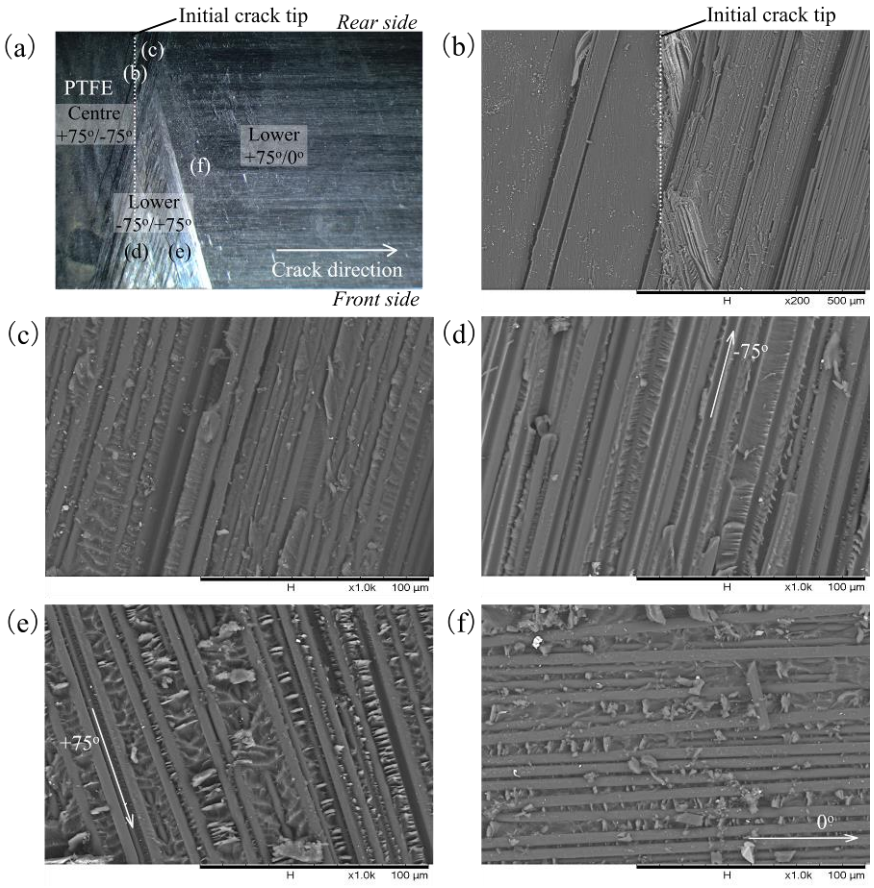

Fig. 20. Micrographs at different locations on the fracture surface from a typical static specimen with θ = 75°.

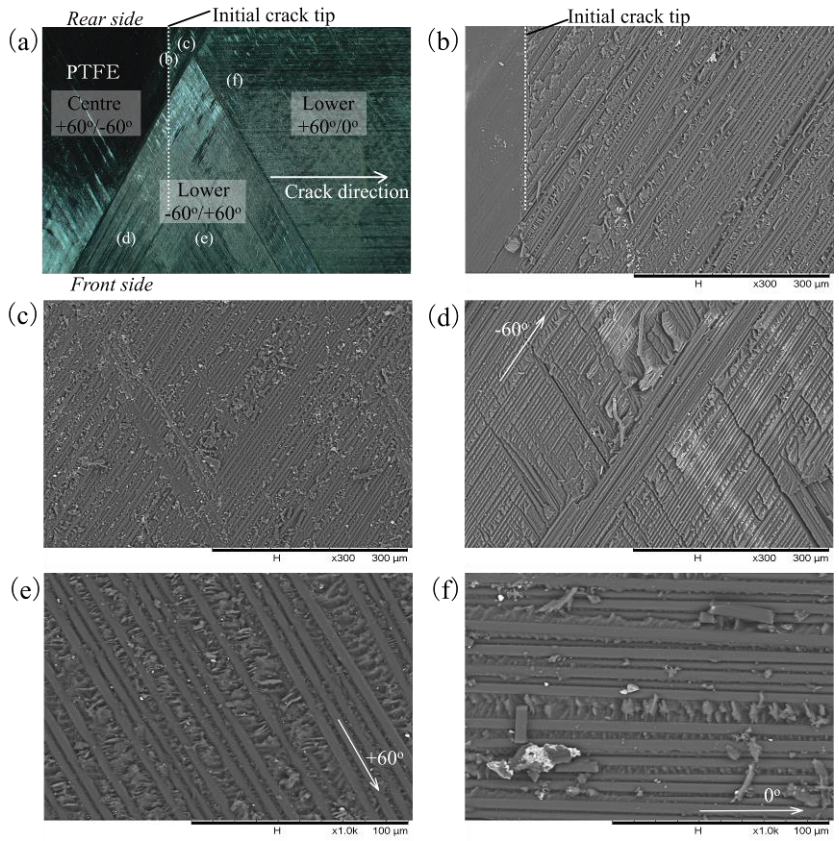

Fig. 21. Micrographs at different locations on the fracture surface from a typical static specimen with θ = 60°.

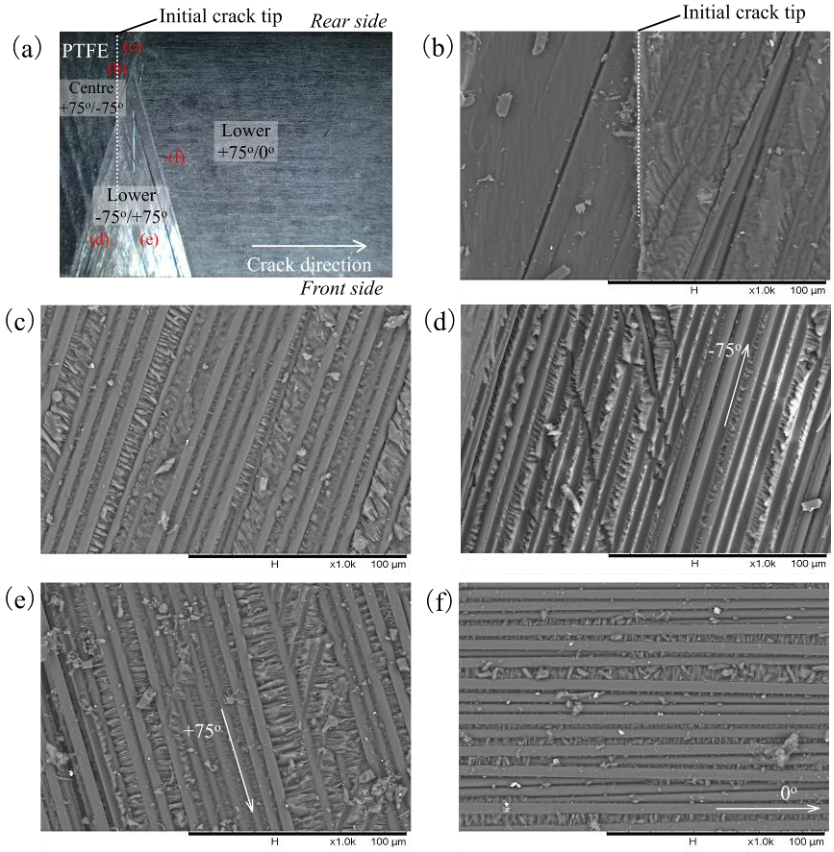

Fig. 22. Micrographs at different locations on the fracture surface from a typical fatigue specimen with θ = 75°.

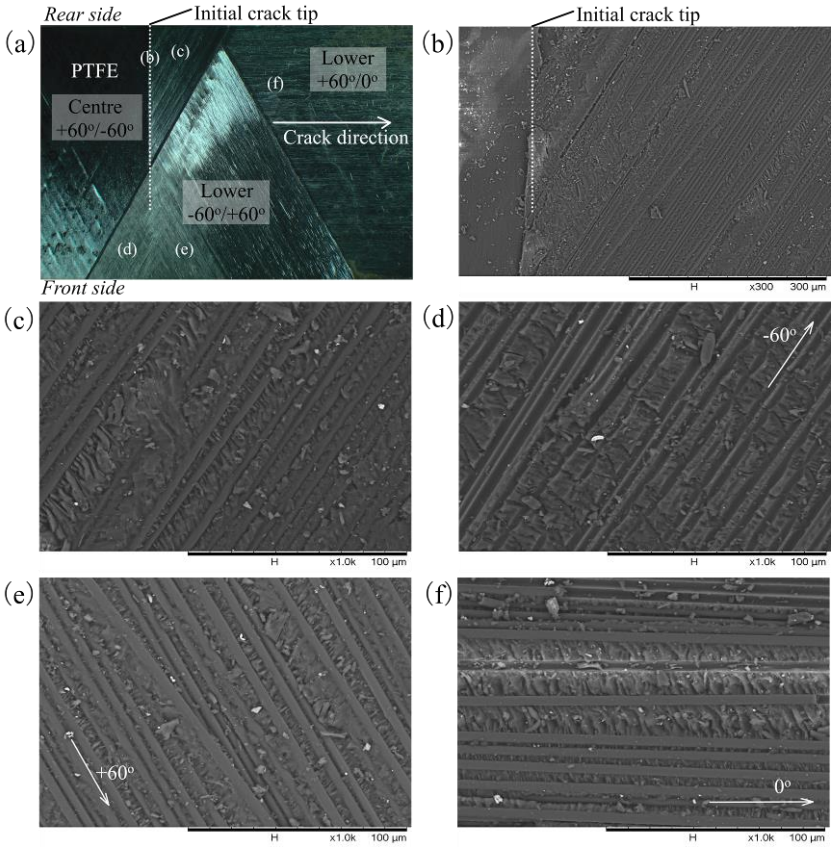

Fig. 23. Micrographs at different locations on the fracture surface from a typical fatigue specimen with θ = 60°.

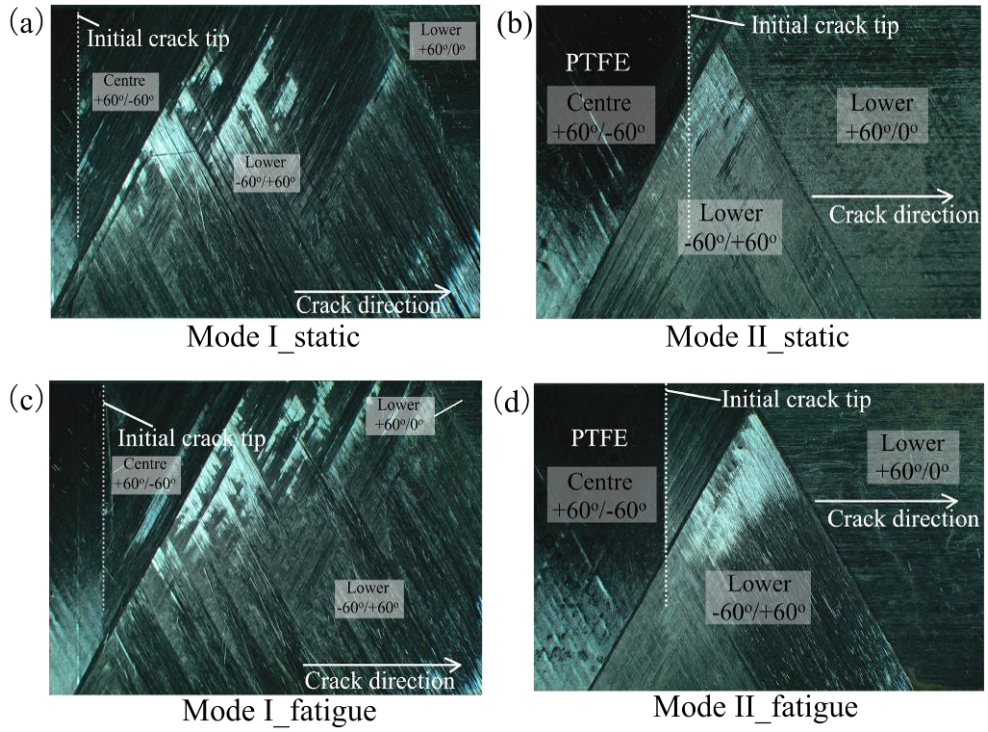

Fig. 24. Summary of the failed fracture surfaces of static and fatigue DCB and ELS specimens with θ = 60°.

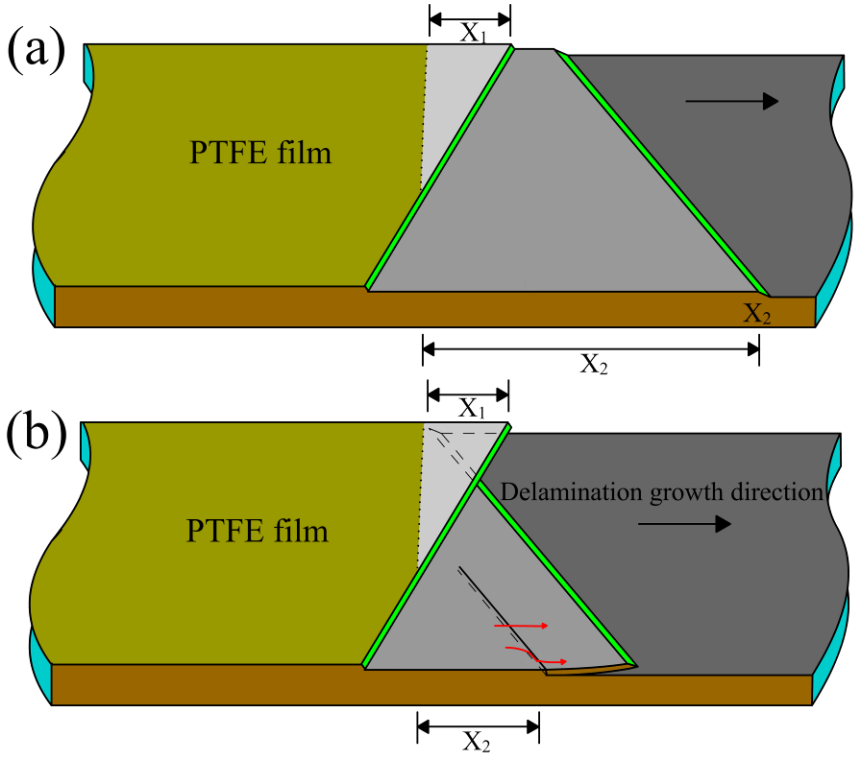

Fig. 25. Sketch of fracture surface from static (a) DCB and (b) ELS specimens with θ = 60°.

Table Captions

Table 1 Number of specimens tested for each configuration; the number of interrupted tests are indicated in parentheses.

Table 2 Distances of migrated points to the PTFE insert front for static (S) and fatigue (F) ELS specimens (Unit: mm).

Table 3 Summary on distances of migrated points to the PTFE insert front (Unit: mm).

Table 1 Number of specimens tested for each configuration; the number of interrupted tests are indicated in parentheses.

	Static test	Fatigue severity		
		40%*	45%	50%
θ = 75°	5(2)	3(3)	1	2
		40%	45%*	50%
θ = 60°	6(3)	3	3(3)	1

Table 2 Distances of migrated points to the PTFE insert front for static (S) and fatigue (F) ELS specimens (Unit: mm).

θ=75°	X_1	$\bar{X}_1$ (S.D.)	X_2	$\bar{X}_2$ (S.D.)	θ=60°	X_1	$\bar{X}_1$ (S.D.)	X_2	$\bar{X}_2$ (S.D.)
S1	1.0	1.2 (0.3)	4.2	4.3 (0.1)	S1	3.4	3.4 (0.1)	9.3	9.0 (1.0)
S2	1.5		4.4		S2	3.4		9.9	
S3	1.2		4.3		S3	3.5		7.9	
F1	1.0	1.0 (0.3)	1.8	1.8 (0.2)	F1	6.5	6.4 (0.5)	6.3	6.5 (0.7)
F2	0.8		2.0		F2	5.9		5.9	
F3	1.3		1.6		F3	6.8		7.2	

Table 3 Summary on distances of migrated points to the PTFE insert front (Unit: mm).

	θ = 75°	$\bar{X}_1$ (S.D.)	$\bar{X}_2$ (S.D.)	θ = 60°	$\bar{X}_1$ (S.D.)	$\bar{X}_2$ (S.D.)
Static	Mode I	3.9(1.2)	5.4(0.1)	Mode I	12.3(2.5)	32.3(0.6)
	Mode II	1.2(0.3)	4.3(0.1)	Mode II	3.4(0.1)	9.0(1.0)
Fatigue	Mode I	3.0(0.8)	3.9(0.6)	Mode I	10.5(0.9)	31.0(1.8)
	Mode II	1.0(0.3)	1.8(0.2)	Mode II	6.4(0.5)	6.5(0.7)